JCIM JOURNAL OF CHEMICAL INFORMATION AND MODELING

pubs.acs.org/jcim Article

Binding Mechanism of UAMC-1110 to Fibroblast Activation Protein

Joep W. Wals, Rui P. P. Neves, Pedro A. Fernandes, and Hans De Winter*

Cite This: J. Chem. Inf. Model. 2026, 66, 7179−7189 Read Online

ACCESS | Metrics & More | Article Recommendations | Supporting Information

ABSTRACT: Fibroblast activation protein (FAP) is an enzyme highly expressed in cancer-associated fibroblasts. Over the past years, several FAP inhibitors (FAPIs) have been developed for tumor imaging. These approaches typically involve covalently linking a metal-loaded chelator to a small molecule ligand that targets FAP. Prolonged tumor retention of FAPIs is desirable to support theranostic applications, which integrate both diagnostic and therapeutic functions. Therefore, we sought to elucidate the binding mechanism of our in-house−designed FAPI lead compound, UAMC-1110. Initial molecular dynamics simulations yielded a noncovalent binding pose of the ligand. Subsequently, QM/MM calculations were performed to investigate the covalent binding mechanism of UAMC-1110. Our results corroborate that the compound forms a covalent complex with the receptor through a reaction pathway that begins with proton transfer from S624 to H734, followed by a concerted, asynchronous nucleophilic attack of S624 on the nitrile warhead. The resulting imidate anion is stabilized via two possible routes: (1) protonation mediated by H734 through two water molecules, and (2) direct protonation by Y541 followed by reprotonation. Covalent MD simulations reveal that H734 interacts more frequently with the imidate anion than Y541, identifying a previously unrecognized and kinetically favored protonation pathway via H734, further supported by water-density and Gibbs energy calculations. Simulations of the final product state additionally indicate that neither residue remains in proximity to the covalent adduct, making reversibility of the reaction complex unlikely and instead suggesting hydrolysis as the most plausible mechanism for complex dissociation.

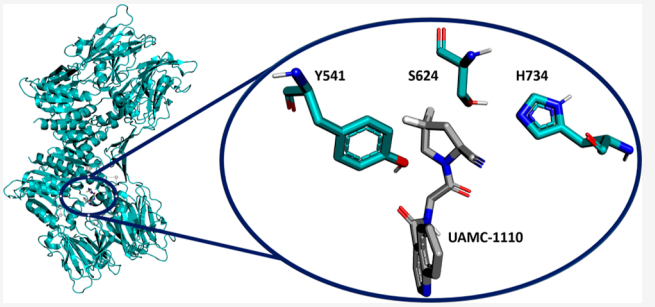

INTRODUCTION

Fibroblast activation protein α (FAP) is a serine protease that is highly expressed in cancer-associated fibroblasts (CAFs),[1] making it an interesting pharmaceutical target. UAMC-1110, a compound developed in our group (Scheme 1), was the first reported fibroblast activation protein inhibitor (FAPI).[2] To enable its use as a diagnostic agent, this compound was chemically conjugated to a DOTA chelator for radiometal labeling. One such derivative, [^{68}Ga]-FAPI-46, is currently used clinically for tumor diagnosis in patients.[3]

Scheme 1. Chemical structure of UAMC-1110

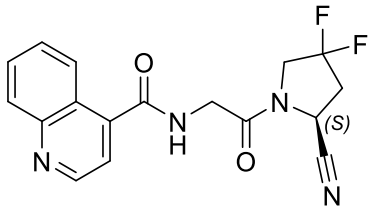

By varying the coordinated metal atom and/or chelator, the same compound can be adapted for different applications, including therapeutics, diagnostics, or a combination of both, commonly referred to as *theranostics*. For instance, [^{68}Ga]-FAPI-46 is used for tumor imaging, whereas its therapeutic counterpart, [^{177}Lu]-FAPI-46, is employed for treatment.[3] In 2022, the first theranostic drug was approved by the FDA and EMA: [^{177}Lu]-PSMA-617 demonstrated high efficacy and low side effects in the treatment of prostate cancer in patients who had undergone extensive prior therapies.[4]

Despite this initial therapeutic success, translating theranostics to FAP-targeted systems remains challenging, and to date, no FAP-directed theranostic drugs have been approved by the EMA and FDA. The relatively short tumor retention time of current compounds represents the major limitation. For therapeutic applications involving radionuclide therapy, the compound must bind strongly to FAP to minimize side effects arising from unbound radiolabeled agents. To achieve strong receptor interactions, FAPIs typically contain a warhead functional group that forms a covalent bond with the catalytic residue S624. In the context of radiotherapy, the covalent interaction should ideally be strong and irreversible. Currently

Received: February 13, 2026
Revised: May 12, 2026
Accepted: May 14, 2026
Published: May 30, 2026

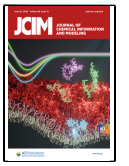

https://doi.org/10.1021/acs.jcim.6c00470
J. Chem. Inf. Model. 2026, 66, 7179−7189

Scheme 2. Overview of the QM Region Comprising UAMC-1110 and Selected Active-Site Residues[a]

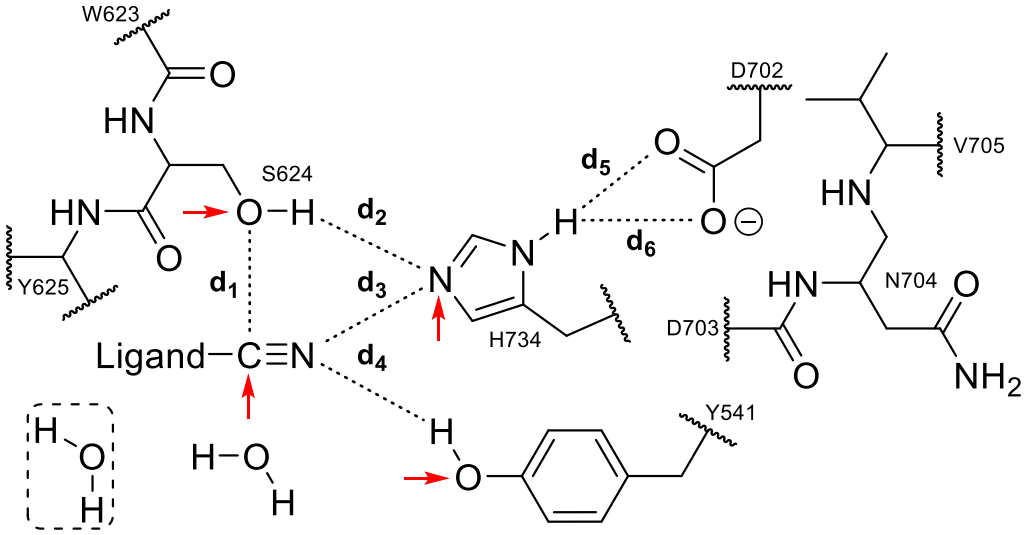

[a]During the first stage of the mechanism, corresponding to the nucleophilic attack, one water molecule is included in the QM region, resulting in a total of 121 atoms. In the second stage of the reaction mechanism, a second water molecule is incorporated, increasing the QM region to 124 atoms. Six distances ($d_1 - d_6$) were analyzed to guide the selection of the starting structure. The four red arrows indicate the atoms defining the reactive center used for truncation.

used nitrile warheads form relatively unstable covalent complexes, resulting in limited tumor retention times. More recently, FAP inhibitors incorporating an α-ketoamide warhead have been developed; these compounds exhibit prolonged tumor retention *in vivo*, underscoring their potential for the development of next-generation FAP-targeted radiopharmaceuticals.[5,6]

To rationalize and optimize the tumor retention time of FAPIs, the underlying reaction mechanism can be investigated using quantum mechanics/molecular mechanics (QM/MM) approaches.[7] The development of such multiscale modeling techniques was recognized with the 2013 Nobel Prize in Chemistry.[8] The methodology combines the high accuracy of quantum mechanics (QM) with the relatively low computational cost of molecular mechanics (MM). For example, Wang and co-workers applied QM/MM molecular dynamics simulations to study the reaction mechanism of vildagliptin and saxagliptin with dipeptidyl peptidase 4 (DPP4), a close homologue of FAP.[9] They identified a concerted mechanism in which H740 is deprotonated by D708 while simultaneously deprotonating S630, thereby enabling nucleophilic attack of S630 on the nitrile warhead to form a covalent bond. The resulting imidate anion is subsequently protonated by Y547 to yield a neutral imidate and a tyrosine anion. This tyrosinate is then reprotonated by the positively charged histidine via two water molecules, as later demonstrated by Corredor et al.,[10] resulting in the more stable neutral products.

Hydrolysis of these products is initiated by nucleophilic attack of a water molecule, forming a tetrahedral intermediate, followed by release of imidic acid and regeneration of the catalytic S630. Collectively, these findings highlight the critical role of the catalytic triad (S630, H740 and D708) in the covalent binding of vildagliptin to DPP4. In addition, Y547 was shown to interact with the imidate product of vildagliptin in a DPP4 crystal structure (PDB: 3W2T).[11] Site-directed mutagenesis studies could be employed to validate the contribution of specific residues to the binding mechanism. For instance, in the case of FAP, substitution of the catalytic serine residue with an alanine has been demonstrated to abolish enzymatic activity.[12] Furthermore, these mechanistic insights could be corrobated through complementary experimental approaches, including high-resolution crystallographic analyses and detailed kinetic assays.[6] To date, no crystal structures of ligands covalently bound to FAP have been reported, nor have QM/MM studies been performed on FAP-targeting inhibitors.

Consequently, given the importance of developing novel FAPIs for theranostic applications, we investigated the detailed binding mechanism of UAMC-1110 to FAP in this work. These mechanistic insights may help guide the rational design of compounds with prolonged tumor retention times. To do so, we resorted to molecular dynamics simulations to model the interaction of FAP with the UAMC-1110 inhibitor and followed with hybrid QM/MM calculations within the ONIOM subtractive scheme to assess the reaction mechanism of the inhibition by the UAMC-1110 inhibitor with atomistic detail, as well as its underlying energetics. We investigated the following aspects: (1) whether UAMC-1110 bind covalently to FAP; (2) the molecular binding mechanism of UAMC-1110 toward FAP; (3) the hydrolysis mechanism of UAMC-1110; and (4) whether the inhibition mechanism of FAP by UAMC-1110 resembles that of DPP4 by vildagliptin and saxagliptin.

METHODS

System Preparation of the Protein−Ligand Complex

The crystal structure of FAP (PDB: 6Y0F) was used as the initial model.[13] As the unit cell contains two dimers, one dimer (chains A and B) was removed. All molecular dynamics (MD) simulations were performed on the remaining dimer, allowing parallel simulation of two ligand−protein interactions, with one ligand bound to each monomer. ModLoop and MolProbity[14,15] were used to model missing residues and optimize hydrogen-bonding networks. Protonation states of ionizable residues at pH 6.3 were assigned based on pK_a predictions obtained with H++ (version 4.0) and PROPKA 3.[16−19] The structure of the UAMC-1110 ligand (Scheme 1) was constructed in PyMOL (version 2.4.1),[20] using the cocrystallized ligand vildagliptin from DPP4 (PDB: 3W2T) as a template.[11] The protein−ligand complex was solvated with TIP3P water molecules in a periodic boundary condition

https://doi.org/10.1021/acs.jcim.6c00470
J. Chem. Inf. Model. 2026, 66, 7179−7189

(PBC) box, with a minimum distance of 10 Å between the protein and box edges,[21] resulting in 64,901 water molecules. Finally, Na^+ and Cl^- ions were added to achieve a physiological salt concentration of 0.15 M.

Molecular Dynamics Simulations on the Protein−Ligand Complex

All MD simulations were performed using AMBER 20, employing the ff14SB force field to describe protein residues and GAFF for the UAMC-1110 ligand.[22−24] Following model construction, the system underwent an energy minimization, after which equilibration was conducted in two stages. First, a 1 ns simulation was performed in the *NVT* ensemble at 300 K, followed by a 1 ns simulation in the *NPT* ensemble at 300 K and 1 bar, using a 2 fs time step.[23,24] Subsequently, three independent production runs of 500 ns each were conducted, yielding a total simulation time of 1.5 μs. All simulation details are provided in the Supporting Information. Because simulations were performed on the dimeric form of FAP with two UAMC-1110 molecules present (one bound to each monomer), the effective sampling corresponds to 3 μs of simulation data. In addition, MD simulations were also performed on FAP complexes containing covalently bound UAMC-1110, both in its anion form (deprotonated imidate; INT1 in Scheme 3) and its neutral form (protonated imidate, PC3 in Scheme 3). The same simulation protocol was applied as for the noncovalent complexes, except that S624 was modified to include a covalent linkage to UAMC-1110.

Starting Structure Selection

Conformations from the MD simulations of the FAP-UAMC-1110 complex were inspected for six key distances (d_1 − d_6, Scheme 2) indicated to be relevant for the inhibition of the DPP4 homologue by previous mechanistic studies on nitrile warheads.[9,10] To identify a suitable starting structure for the QM/MM calculations, conformations were first filtered using a maximum distance cutoff of 4.0 Å for d_1, corresponding to the nucleophilic of S624 on the nitrile warhead. Then, conformations with the smallest cumulative sum of these distances were visually inspected to assess the individual distances. The fourth-ranked conformation was selected as the starting structure, as the three highest-ranked frames exhibited substantially larger values for d_2, corresponding to the hydrogen bond between S624 and H734 conserved in enzymes exhibiting the SHD triad. Finally, the energy of the selected starting conformation was minimized using the same minimization protocol applied in the MD simulations.

QM/MM Calculations

For the QM/MM calculations, the system was truncated to 5772 atoms by selecting all residues and water molecules within 20 Å of a reactive center, defined by the four atoms highlighted in the QM region (Scheme 2). These atoms were selected as reactive because they are proposed to be directly involved in bond cleavage and formation. Residues located beyond a 15 Å radius from the reactive center were frozen, as were all water molecules in the MM region. Covalent bonds crossing the QM/MM boundary were treated using link atoms placed at C−C_α or C_α−C_β bonds. In total, the QM region encompassed 121−124 atoms, with a total net charge of −1 and a singlet multiplicity, and the MM region exhibited a net charge of +2 and doublet multiplicity. The multiplicity of the MM layer was set as doublet because a disulfide bond was severed during truncation. System construction and visual inspection were performed using the molUP extension of VMD (version 1.9.3).[25,26] QM/MM calculations were conducted with Gaussian 16 using the ONIOM QM/MM framework and the electrostatic embedding formalism.[27,28] The QM region was treated with the B3LYP functional and 6−31G(d) basis set, while the MM region was described using the ff14SB force field.[23,29−31] Reaction coordinate scans were performed along tentative reaction coordinates describing the mechanistic hypothesis depicted in Scheme 3, from which tentative stationary states and corresponding energy changes were inspected.[32] Tentative stationary states were subjected to vibrational frequency analysis at the B3LYP/6−31G(d):ff14SB to confirm their nature: minima and transition states were validated by evaluating the number of imaginary frequencies exhibited: null number of imaginary frequencies for minima and a single imaginary frequency for transition states. Transition states were also validated by visual inspection of the normal mode corresponding to the imaginary frequency, which should encompass the atoms involved in bond cleavage and formation. QM and MM parcels of the ONIOM energy of the optimized stationary points were also compared against those of the tentative stationary points retrieved from reaction coordinate scans. Final Gibbs energies for stationary points were calculated at the B3LYP-D3/6−311 + G(2d,2p):ff14SB//B3LYP/6−31G(d):ff14SB level of theory.[33,34]

RESULTS

Forming the Covalent Complex

In our analysis of the covalent reaction mechanism of UAMC-1110 binding to FAP, we assumed that the nitrile warhead of UAMC-1110 is attacked by the catalytically important residue S624 (blue arrows in Scheme 3A). Accordingly, we investigated the energetics of the nucleophilic attack of S624 on the nitrile carbon to form the intermediate structure (Scheme 3A; INT1), as well as two subsequent protonation routes of the resulting imidate anion (Scheme 3B): protonation by Y541 (the "tyrosine pathway" and "tyrosine reprotonation"; orange and red arrows) and protonation by H734 (the "histidine pathway"; green arrows).

During the nucleophilic attack, the catalytic residue H734 deprotonates S624, thereby activating it for nucleophilic attack on the nitrile warhead. This step proceeds in a concerted yet asynchronous manner, yielding the covalent intermediate (INT1). The resulting positively charged H734 forms a stabilizing ionic interaction with D702, highlighting the functional role of the catalytic triad. In addition, two nearby tyrosine residues contribute to stabilization of the anion hole, consistent with previous studies on DPP4.[9,10] Specifically, the imidate anion is stabilized by the backbone of one tyrosine residue and the hydroxyl group of another. Interestingly, additional interactions also appear to play a significant role and are discussed further in the section describing the covalently bound intermediate.

Step 1: Nucleophilic attack. To obtain a suitable starting structure for QM/MM simulations, three independent MD simulations of 500 ns each were performed on the noncovalent protein−ligand complex. Because the dimeric form of FAP was simulated, with one ligand bound to each monomer, this resulted in a total of 3 μs of simulation data. Throughout most of the simulations, the ligands displayed substantial conformational flexibility, as reflected by the root-mean-square-deviation (RMSD) analysis (Figure S1). In one of the three trajectories, an unbinding event was observed for one of the two UAMC-1110 molecules via the side opening of FAP, which has an approximate diameter of 24 Å and is significantly wider than the β-propeller opening (around 14 Å).[35] The nucleophilic attack leading to the formation of INT1 is associated with a Gibbs energy barrier of 8.4 kcal/mol (Figure 1A; blue line) and a Gibbs reaction energy of 7.0 kcal/mol, resulting in a shallow reverse Gibbs energy barrier of 1.4 kcal/mol. Comparable Gibbs energy barriers ($\Delta G^{\ddagger}$) have been reported for nitrile inhibitors binding to DPP4. Wang and co-workers determined Gibbs energy barriers of 8.5 and 10.4 kcal/mol for vildagliptin and saxagliptin, respectively (Figure S2) using QM/MM MD at the DFT/M06−2X:ff99SB level of theory.[9]

Step 2: Protonation of the imidate anion. Next, we investigated the protonation of the imidate anion via two distinct routes (Scheme 3B). The first route comprises the tyrosine pathway followed by the tyrosine reprotonation. In the

https://doi.org/10.1021/acs.jcim.6c00470
J. Chem. Inf. Model. 2026, 66, 7179−7189

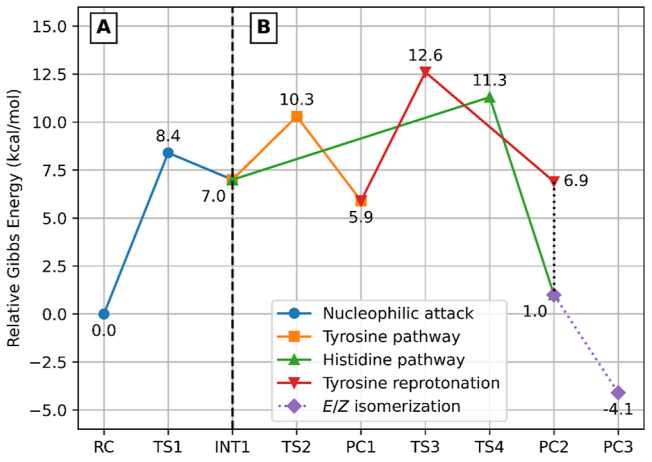

Figure 1. Gibbs energy profile for the binding of UAMC-1110 to FAP. The QM layer for the nucleophilic attack step (A) includes one water molecule, whereas from INT1 onward (B), two water molecules are included. The vertical dotted line at INT1 indicates the change in the QM region from inclusion of the second water molecule, while the vertical dotted line at PC2 denotes two different conformations for PC2. The dotted purple line between PC2 and PC3 indicates the formation of a more stable tautomer (Figure S3). RC = reactant complex, TS = transition state, INT = intermediate, PC = product complex.

tyrosine pathway, the imidate anion is directly protonated by the neighboring Y541, resulting in the formation of a tyrosinate species in the product complex 1 (PC1). The calculated Gibbs energy barrier for this step is 3.3 kcal/mol (Scheme 3B and Figure 1B; orange line), which is higher than the values reported for DPP4 by Wang and co-workers, yet still indicative of a fast process.[9] In their study, negligible Gibbs energy barriers of 0.4 and 0.6 kcal/mol were found for vildagliptin and saxagliptin, respectively (Figure S2). The tyrosine pathway was also investigated by Corredor et al. for vildagliptin bound to DPP4 using QM/MM methods at the DFTB3:CHARMM-36 level of theory, with single-point energy corrections computed at the DFT/M06−2X/6−31g(d) level of theory.[10] In that study, no stable intermediate was identified, and a substantially higher Gibbs energy barrier of 24.7 kcal/mol was reported because their reactant state was strongly stabilized by hydrogen bonding interactions between catalytic residues and nearby water molecules. In the subsequent tyrosine reprotonation, the neutral (acidic) form of Y541 is regenerated in product complex 2 (PC2) via proton transfer from the positively charged H734 through two water molecules (Scheme 3B and Figure 1B; red line). The calculated Gibbs energy barrier for the process is 6.7 kcal/mol, which is considerably lower than the corresponding Gibbs energy barrier of 13.7 kcal/mol reported by Corredor and co-workers (Figure S2).[10] These results highlight that the inhibition of DPP4 by vildagliptin follows a similar mechanism as that verified for the inhibition of FAP by UAMC-1110.

While the tyrosine pathway and tyrosine reprotonation are well documented in the literature, the second protonation route—the histidine pathway—has, to the best of our knowledge, not been previously investigated for related serine proteases such as DPP4. Nevertheless, several studies have examined protonation of the imidate anion in other systems.[36−46] In this direct pathway, H734 protonates the imidate anion via two intervening water molecules, with a calculated Gibbs energy barrier of 4.3 kcal/mol (Figure 1B and Scheme 3B; green line). This route exhibits a lower overall activation free energy than the first route, which has a cumulative barrier of 5.6 kcal/mol (TS3−INT1), and it leads to a more stable PC2, with a Gibbs energy of 6.0 kcal/mol lower than that of the anionic intermediate INT1. Based on these QM/MM results, we interpret that both protonation routes are kinetically feasible, although the histidine route is thermodynamically favorable.

To gain further insight into the dynamic behavior of imidate anion protonation, covalent MD simulations were performed. In these simulations, S624 was modified to covalently bind UAMC-1110 in its anionic imidate form. As before, three independent simulations of 500 ns each were conducted, resulting in a total of 3 μs of simulation data due to the dimeric nature of the system. The role of water molecules in the protonation process was examined by analyzing water density distributions near the imidate anion. A pronounced increase in water density was observed in regions proximal to both H734 and the imidate anion (Figure 2), supporting the feasibility of proton transfer via water-mediated pathways. In contrast, protonation by Y541

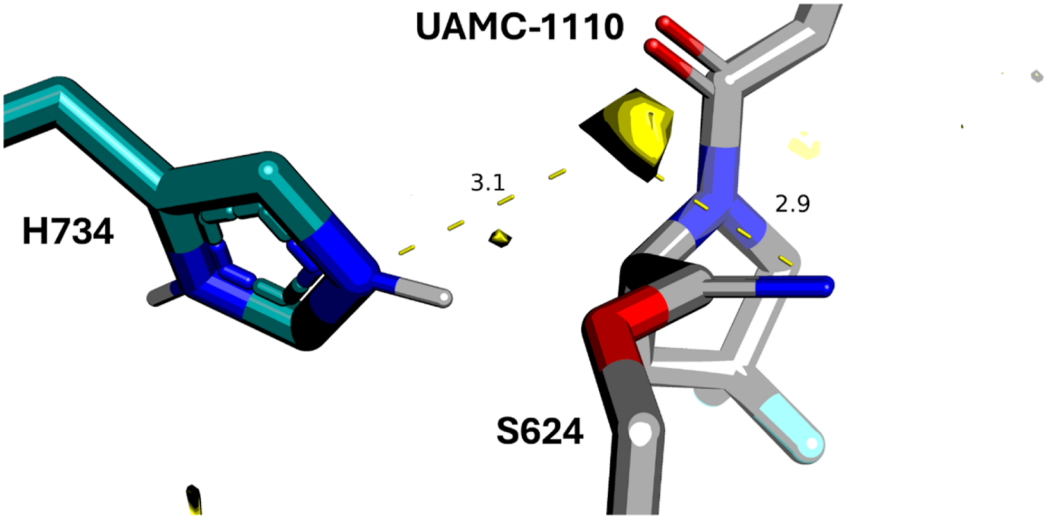

Figure 2. Water density distribution around the imidate anion (INT1), shown as yellow isosurfaces. The ligand is depicted in grey, and H734 is shown in cyan. The distances are indicated in Ångström.

https://doi.org/10.1021/acs.jcim.6c00470
J. Chem. Inf. Model. 2026, 66, 7179−7189

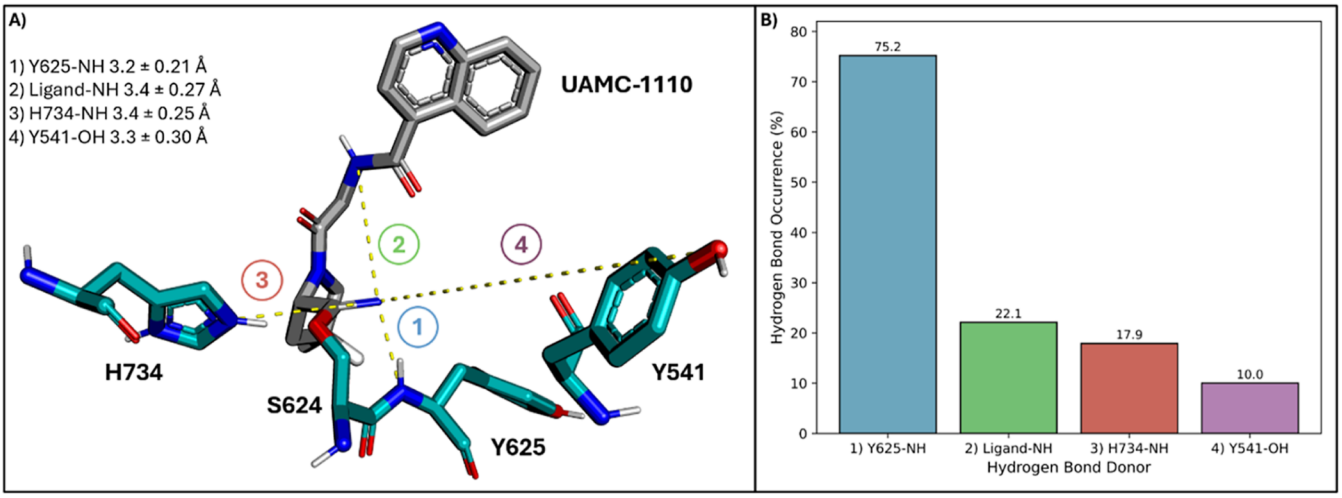

Figure 3. (A) Snapshot of a binding pose of INT1 illustrating the four potential hydrogen bond interactions involving the imidate anion. Distances shown correspond to the mean and standard deviation computed over the time intervals during which the hydrogen bonds were present. The ligand is depicted in grey, while the residues H734, Y625, and Y541 are shown in cyan from left to right. (B) Occurrence of hydrogen bonds involving the imidate anion over the course of the simulations. Hydrogen bonds were defined using a donor−acceptor heavy-atom distance cutoff of 4.0 Å and a minimum acceptor-hydrogen-donor angle of 120°.

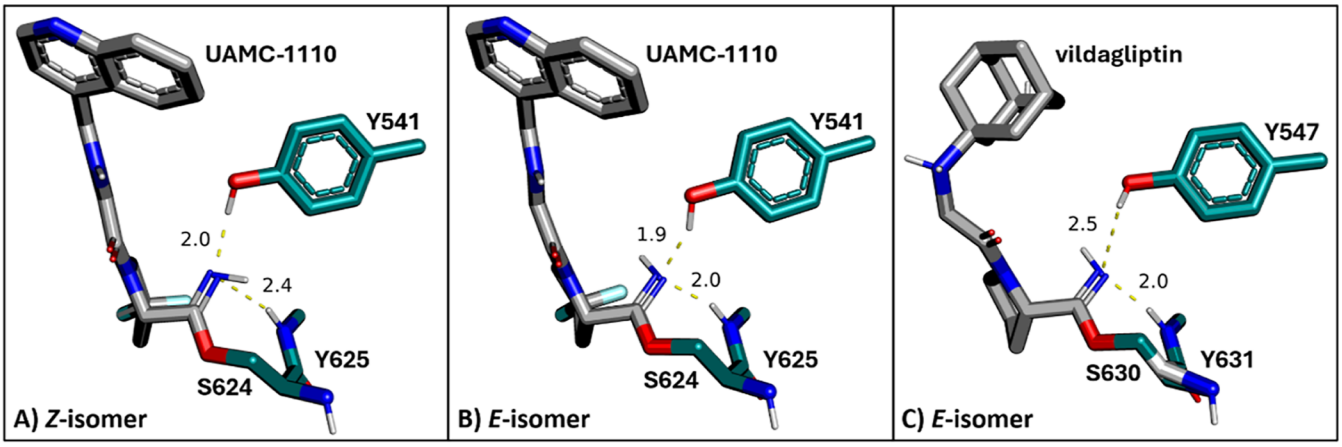

Figure 4. Comparison of the *E* and *Z* imidate configurations. (A) QM/MM-optimized structure of product complex 2 (PC2), showing the *Z* configuration of the imidate. (B) Product complex 3 (PC3) obtained after 180° dihedral rotation, yielding the *E* configuration. (C) *E*-configured imidate of vildagliptin in DPP4 (PC3) as reported by Corredor and co-workers.[10] All distances are shown in Ångström.

appears less likely to involve water molecules, as no significant water density was detected bridging the imidate anion and Y541.

To further investigate the availability of potential proton donors toward the imidate anion, we analyzed the occurrence of nearby hydrogen bond donors and considered the acidity of the corresponding residues. Four hydrogen bonds were identified (Figure 3A): (1) a hydrogen bond with the backbone NH of Y625, (2) an intramolecular hydrogen bond involving the amide NH at the 4-position of the quinoline ring, (3) a hydrogen bond with the N_{ε}-H of H734, and (4) a hydrogen bond with the hydroxyl group of Y541. Analysis of the full 3 μs simulation data set revealed that the most prevalent hydrogen bond is formed with the Y625-backbone (Figure 3B). However, because amide hydrogens are very weak acids,[47] proton transfer from this group is unlikely. The same reasoning applies to the intramolecular hydrogen bond. Notably, the imidate anion forms a hydrogen bond with H734 more frequently than with Y541. This observation suggests that protonation of the imidate anion via H734 is more likely than via Y625, either directly or mediated by a short chain of water molecules.

Step 3: Imidate *E*/*Z* isomerization. Both reprotonation routes yield a configuration in which the reprotonated imidate hydrogen adopts the *Z* configuration of the C═N bond, pointing toward the backbone hydrogen of Y625 and resulting in electrostatic repulsion between the two hydrogens (Figure 4A). We found that rotation of the imidate hydrogen by 180° to form the *E* configuration alleviates this repulsion and enables formation of favorable hydrogen bond with the Y625 backbone (Figure 4B). This conformation is consistent with the imidate geometry observed in the DPP4/vildagliptin complex reported by Corredor and co-workers (Figure 4C).[10] To further examine this process, we performed a dihedral scan around the imidate C═N bond and found that the *E* configuration is 5.1 kcal/mol more stable than the original *Z* form (Scheme 3B and Figure 1B; purple arrows/line). However, direct torsional rotation of the proton from the *Z* to *E* configuration is unlikely due to the high rotational Gibbs energy barrier of the C═N double bond of 18.8 kcal/mol (Figure S3). We therefore propose that the proton flip may occur via a water-mediated proton mechanism, similar to what has been reported for oximes.[48]

https://doi.org/10.1021/acs.jcim.6c00470
J. Chem. Inf. Model. 2026, 66, 7179−7189

Scheme 3. Proposed Reaction Mechanism of UAMC-1110 in FAP[a]

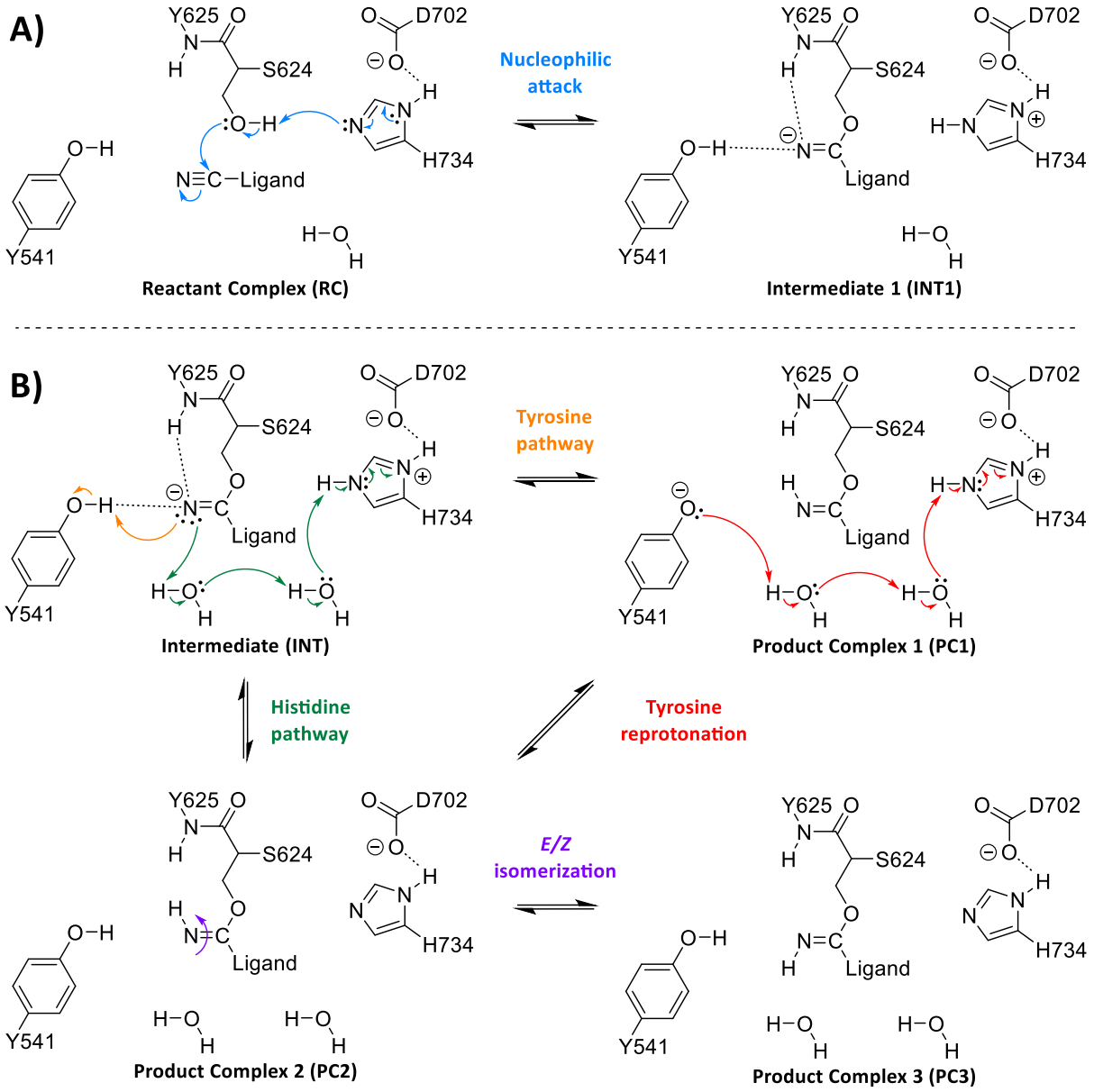

[a](A) Nucleophilic attack of S624 on the nitrile warhead, resulting in the formation of the imidate anion intermediate (INT1). (B) Subsequent protonation of the imidate anion via two possible routes: the tyrosine pathway involving Y541 followed by reprotonation, or the histidine pathway involving H734. Subsequent *E*/*Z* isomerization can yield a more favorable tautomer, designated PC3.

The Covalently Bound Intermediate

To determine which product conformation (PC2 or PC3) is preferentially formed upon protonation of the imidate anion by either H734 or Y541, we analyzed the orientation of the imidate group relative to these residues. Specifically, two dihedral angles were measured when a hydrogen bond was formed between the N═C−O moiety of the imidate (highlighted in Figure 4) and the donating hydrogen of either H734 (imidazolium) or Y541 (hydroxyl), using a 4.0 Å cutoff (Figure S4). This analysis revealed a mean dihedral angle of 319 ± 9° for H734, which closely resembles the orientation observed in PC2 (approximately 360°). In contrast, the dihedral angle associated with Y541 was 182 ± 77°, consistent with the geometry of PC3 (approximately 180°) but exhibiting a much broader distribution. Based on the narrower dihedral distribution for H734, its more frequent proximity to the imidate anion, and the more favorable kinetics indicated by our ONIOM calculations, again protonation by H734 appears to be the preferred pathway.

The Reverse Reaction

To investigate potential pathways for the reverse reaction from PC3 to INT1, we analyzed hydrogen bond interactions involving the imidate group in PC3. For this purpose, three independent MD simulations of 500 ns each were performed, yielding 1.5 μs simulation data and a total of 3 μs of sampling due to the dimeric nature of the system. Our analysis showed that the imidate functions as a hydrogen bond donor only toward two intramolecular acceptors: the amide oxygen of the pyrrolidine moiety and the fluorine substitution on the same ring (Figure 5). Given the low pK_a values of protonated amide oxygen, protonated fluorine, and the imidate group, these intramolecular acceptors are highly unlikely to act as bases capable of

https://doi.org/10.1021/acs.jcim.6c00470
J. Chem. Inf. Model. 2026, 66, 7179−7189

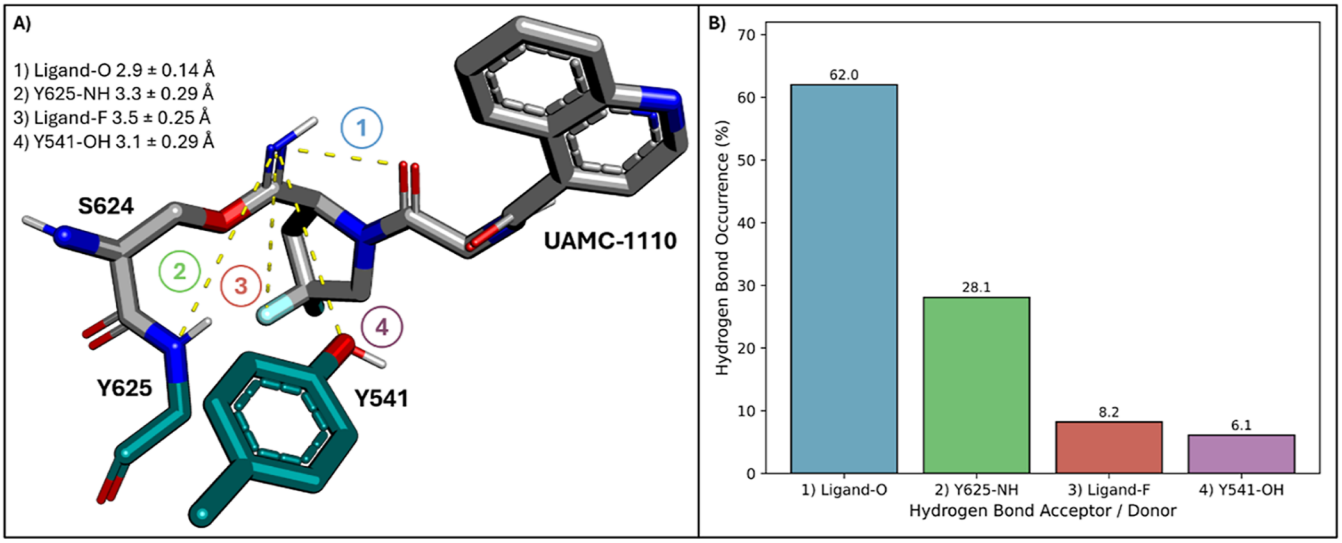

Figure 5. (A) Snapshot of a binding pose of PC3 illustrating the four potential hydrogen bond interactions involving the imidate group. Distances shown correspond to the mean and standard deviation computed over the time intervals during which the hydrogen bonds were present. The ligand is depicted in grey, while residues Y625 and Y541 are shown in cyan from left to right. (B) Hydrogen bonding events involving the imidate group over the course of the simulations. Hydrogen bonds were defined using a maximum donor−acceptor heavy-atom distance of 4.0 Å and a minimum angle of 120°. The imidate acts as a hydrogen bond donor in the two intramolecular interactions, whereas it serves as a hydrogen bond acceptor when interacting with either Y625 or Y541.

Scheme 4. Proposed Hydrolysis Mechanism of UAMC-1110 in FAP[a]

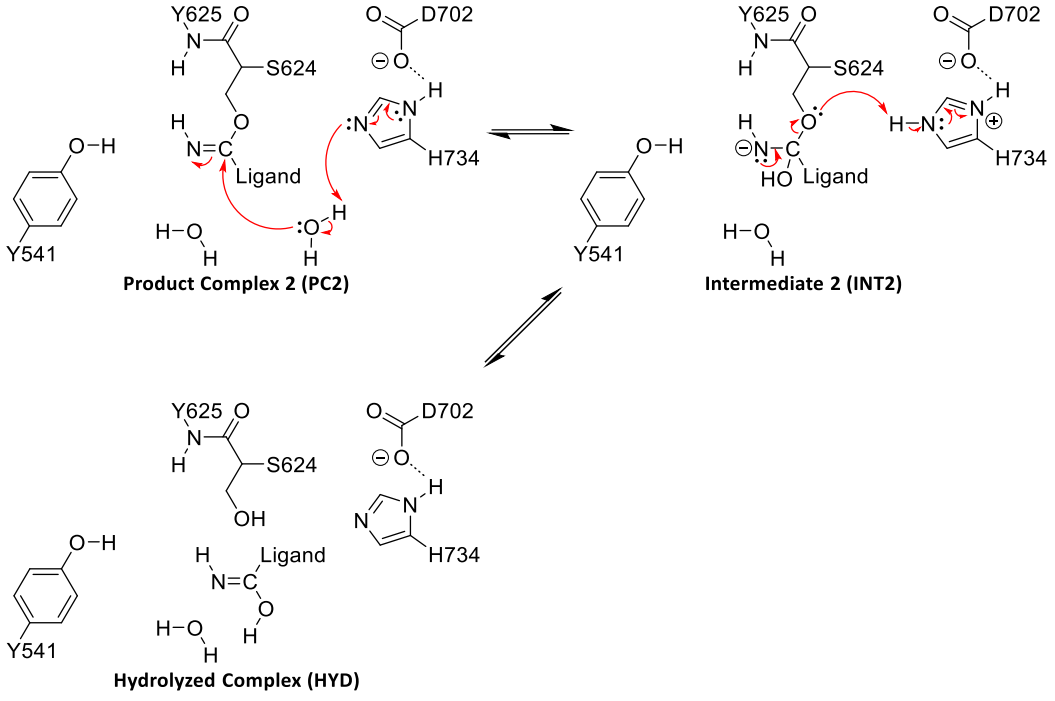

[a]The nucleophilic attack of a water molecule on the imidate group leads to the formation of a tetrahedral intermediate (INT2). In the subsequent step, imidic acid is formed as the catalytic residue S624 acts as the leaving group, yielding the hydrolyzed complex (HYD).

deprotonating the imidate. Consequently, they are unlikely to participate in the reverse reaction from PC3 back to INT1. No hydrogen bond donor interactions between the imidate and the active site residues were observed during the simulations. Although residues Y625 and Y541 occasionally formed hydrogen bonds with the imidate, in these interactions the imidate exclusively acted as a hydrogen bond acceptor rather than a donor.

Collectively, these findings strongly suggest that direct proton transfer from the imidate to the protein is unlikely in the reverse pathway from PC3 to INT1. To further exclude the possibility of a water-mediated proton transfer, we analyzed the water density between the imidate group and either H734 or Y541. No significant water density was observed bridging the imidate with H734 or Y541 (Figure S5), thereby ruling out a water-mediated proton transfer mechanism. These results support the conclusion that the reverse reaction is more likely initiated

https://doi.org/10.1021/acs.jcim.6c00470
J. Chem. Inf. Model. 2026, 66, 7179−7189

through a hydrolysis mechanism, in which a water molecule acts as the nucleophile to trigger reversal of the covalent complex.

Hydrolysis

Because hydrolysis was investigated prior to identification of PC3, the reaction was initially modeled with a water molecule performing a nucleophilic attack on the imidate of product complex 2 (PC2), leading to formation of a tetrahedral intermediate (INT2; Scheme 4) This step is associated with a Gibbs energy barrier of 17.9 kcal/mol, and the resulting intermediate has a Gibbs energy of 13.6 kcal/mol relative to the reactant state (Figure 6). In the subsequent step, imidic acid is

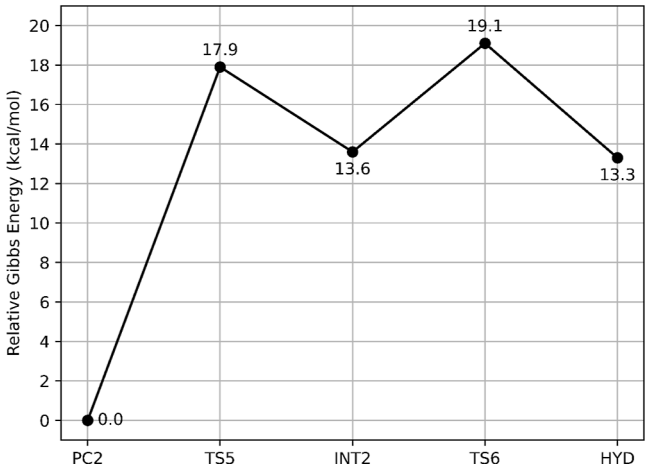

Figure 6. Gibbs energy profile for the hydrolysis of UAMC-1110 in FAP. PC = product complex, TS = transition state, INT = intermediate, HYD = hydrolyzed complex.

formed as the catalytic residue S624 acts as the leaving group, corresponding to an Gibbs energy barrier of 5.5 kcal/mol and yielding a hydrolyzed complex (HYD) with a Gibbs energy of 13.3 kcal/mol. Comparable studies on vildagliptin and saxagliptin bound to DPP4 have reported Gibbs energy barriers ranging from 17.6 to 34.6 kcal/mol for the initial nucleophilic attack on PC3 (Figure S6), as well as Gibbs reaction energies between 0.9 and 22.5 kcal/mol for the resulting hydrolyzed complexes (HYD). Based on the water densities that we found surrounding the imine moiety on our MD simulations (Figure S5), we hypothesize that the water-mediated tautomerization from the resulting imine (HYD) to the amide form should be a kinetically favored process, leading to a more exergonic outcome.[49,50] Nevertheless, a thorough discussion on this subject was beyond the scope of the present study.

Improving Residence Time

As discussed above, hydrolysis is favored over the reverse covalent pathway. In both scenarios, the magnitude of the Gibbs energy barrier governs the dissociation rate of UAMC-1110 from FAP, and consequently its residence time. Therefore, enhancing protein−ligand interactions is expected to increase residence time.

Structure−activity relationship (SAR) studies have highlighted the pivotal role of the proline-derived 2-cyano-4,4-difluoropyrrolidine moiety, which is linked via an amide bond to the quinoline scaffold.[2,51] In addition, systematic variation of substituents on the quinoline ring has been investigated, with contemporary FAP inhibitors typically incorporating a linker at the 6′-position. Notably, relocation of the quinoline nitrogen significantly reduces binding affinity.[51] Introduction of an additional nitrogen atom has thus far only been explored in a 1,7-naphthyridine analogue, which resulted in an approximately 3-fold decrease in affinity.[2]

Covalent MD simulations (PC3 model) revealed stabilizing cation−π interactions between the quinoline ring and residue R123. These findings suggests that strategic incorporation of an additional nitrogen atom at alternative positions on the heteroaromatic scaffold may enhance residence time by strengthening cation−π interactions with the guanidinium moiety of R123. Positional analysis indicates that replacement of the 3′ and/or 8′ carbon positions is most promising, as these sites are more frequently located in close proximity to the primary arginine nitrogens (Figure S7). In contrast, carbon replacement of the 2′ position is unlikely to yield substantial improvements, as its interaction profile closely resembles that of the native 1′ position. The 5′, 6′ and 7′ positions are spatially more distal from the R123 guanidine group and are therefore less favorable.

Replacement of the quinoline core with alternative heterocycles such as quinazoline, 1,8-naphthyridine, or pyrido[2,3-*d*]pyrimidine appears synthetically accessible. However, while such modifications may confer modest improvements in residence time, their overall impact is expected to be less pronounced than that achieved by substitution of the nitrile warhead with an α-ketoamide.[5,6]

CONCLUSION

In this study, we investigated the reaction mechanism of UAMC-1110 binding to FAP, which involves nucleophilic attack by S624 followed by protonation of the resulting imidate anion. The Gibbs energy barrier for the nucleophilic attack was calculated to be 8.4 kcal/mol, in agreement with previous studies on nitrile inhibitors targeting the homologous protein DPP4.[9] Covalent MD simulations revealed that the intermediate is primarily stabilized by a hydrogen bond with the backbone of Y625. In addition, H734 forms hydrogen bonds with the imidate anion more frequently than Y541, suggesting a previously unrecognized protonation route via H734 for nitrile warheads binding to FAP and related serine proteases.

Our results indicate that this pathway is less likely than protonation via H734, based on the more favorable kinetics and orientation of the latter mechanism. Water density analyses further support this conclusion, revealing a higher probability of water molecules positioned between H734 and the imidate anion. These findings are consistent with our QM/MM calculations, which show favorable Gibbs energy barriers for both protonation via H734 mediated by water molecules and direct protonation by Y541 followed by reprotonation via water.

Covalent MD simulations of the PC3 intermediate indicate that neither Y541 nor H734 remains in close proximity to the covalently bound inhibitor. This spatial separation renders the reverse reaction from PC3 to the initial reaction complex unlikely, thereby supporting hydrolysis as the more plausible pathway for complex dissociation. Future investigations employing QM/MM molecular dynamics simulations could provide a more detailed characterization of imidate protonation dynamics. Such approaches would enable a more accurate assessment of the preferred protonation pathway, if any, and well as the associated reverse Gibbs free energy barrier. By yielding a more reliable description of the binding kinetics of UAMC-1110, these computational results could be directly compared with existing experimental kinetic data to further validate the proposed mechanistic framework.

https://doi.org/10.1021/acs.jcim.6c00470
J. Chem. Inf. Model. 2026, 66, 7179−7189

■ ASSOCIATED CONTENT

Data Availability Statement

System setup files and molecular dynamics parameter files for the (covalent) MD simulations using Amber 20 are provided in the Supporting Information (SI_MD_System_Preparation and SI_MD_Input_Files.zip). ModLoop, MolProbity and H++, are freely available Web servers accessible at https://modbase.compbio.ucsf.edu/modloop/, http://molprobity.biochem.duke.edu/ and http://newbiophysics.cs.vt.edu/H++/. PROPKA 3 is released under the GNU Lesser General Public License v2.1 and is available at https://propka.readthedocs.io/en/latest/index.html. The (covalent) MD simulations were performed with the AMBER 2020 and AmberTools 20 software (https://ambermd.org/GetAmber.php). AmberTools 20 is freely available for download, whereas AMBER 20 is available free of charge only for academic use. Data analysis was performed using CPPTRAJ, which is part of AmberTools 20. Visual analysis was performed using PyMol, for which a license was acquired from (https://www.pymol.org/). QM/MM calculations were performed using the Gaussian 16 software, which requires the purchase of an academic license (https://gaussian.com/gaussian16/). Visual analysis was performed using PyMol, VMD and its extension molUP. VMD is freely available for download at https://www.ks.uiuc.edu/Development/Download/download.cgi?PackageName=VMD, and molUP is released under the MIT license and is available at https://github.com/BioSIM-Research-Group/molUP. QM/MM input files are provided in the Supporting Information (SI_QM-MM_Input_Files.zip). In-house python scripts were developed using Python 3.0, available free of charge at https://www.python.org/download/releases/3.0/, and the python modules matplotlib (https://matplotlib.org/3.5.3/index.html) and numpy (https://numpy.org/).

Supporting Information

The Supporting Information is available free of charge at https://pubs.acs.org/doi/10.1021/acs.jcim.6c00470.

The system preparation files for MD simulations are provided in SI_MD_System_Preparation (ZIP)

The QM/MM files are provided in SI_QM-MM_Input_Files.zip (ZIP)

The QM/MM stationary points (PDB) are provided in SI_QM-MM_Stationary_Points.zip (ZIP)

The detailed methods describing the system preparation, MD simulations, analysis of the MD simulations, and QM/MM calculations are provided in the Supporting Information. The Supporting Information involves different figures and tables Figure S1. RMSD of the two UAMC-1110 molecules bound to the FAP dimer over the course of the MD simulation. Figure S2. Comparison of obtained QM/MM results with other studies. Figure S3. Gibbs energy profile of the *E*/*Z* isomerization from PC2 to PC3 of UAMC-1110. Figure S4. Rose plot of two different dihedrals of the covalent MD on the intermediate (INT1). Figure S5. Water density distribution around the imidate (PC3), shown as yellow isosurfaces. Figure S6. Comparison of obtained QM/MM hydrolysis results with other studies. Figure S7. Occurrence of distances involving R123 and the quinoline atoms over the course of the simulations. Table S1. Reaction coordinate scans for each pathway. Table S2. The specific bonds defining the reaction coordinate scans of the different pathways. Table S3. Imaginary frequencies for the transition states of each pathway (PDF)

■ AUTHOR INFORMATION

Corresponding Author

Hans De Winter − *Laboratory of Medicinal Chemistry, Department of Pharmaceutical Sciences, University of Antwerp, 2610 Wilrijk, Belgium;* orcid.org/0000-0002-4450-7677; Email: hans.dewinter@uantwerpen.be

Authors

Joep W. Wals − *Laboratory of Medicinal Chemistry, Department of Pharmaceutical Sciences, University of Antwerp, 2610 Wilrijk, Belgium;* orcid.org/0000-0002-6439-0453

Rui P. P. Neves − *LAQV@REQUIMTE, Departamento de Química e Bioquímica, Faculdade de Ciências, Universidade do Porto, 4169-007 Porto, Portugal;* orcid.org/0000-0003-2032-9308

Pedro A. Fernandes − *LAQV@REQUIMTE, Departamento de Química e Bioquímica, Faculdade de Ciências, Universidade do Porto, 4169-007 Porto, Portugal;* orcid.org/0000-0003-2748-4722

Complete contact information is available at: https://pubs.acs.org/10.1021/acs.jcim.6c00470

Author Contributions

Joep W. Wals: Conceptualization, Data Curation (lead), Formal Analysis (lead), Funding Acquisition (lead), Investigation (lead), Methodology, Project Administration, Software (lead), Validation (lead), Visualization (lead), Writing—Original Draft Preparation (lead), Writing—Review & Editing (lead). **Rui P. P. Neves**: Conceptualization, Formal Analysis, Methodology (lead), Supervision (lead), Validation, Writing—Review & Editing (lead). **Pedro A. Fernandes**: Conceptualization, Methodology, Resources, Supervision, Writing—Review & Editing. **Hans De Winter**: Conceptualization (lead), Funding Acquisition, Methodology, Project Administration (lead), Resources (lead), Supervision (lead), Writing—Review & Editing (lead).

Notes

The authors declare no competing financial interest.

■ ACKNOWLEDGMENTS

J.W.W. received a travel grant from the Fonds Wetenschappelijk Onderzoek Grant V427319N. The computational resources for this project were provided by the VSC (Flemish Supercomputer Center; gpr_compute_2023_037) and the EuroCC Belgium (LUMI-BE; project_465000650). R.P.P.N. thanks FCT for funding through the Individual Call to Scientific Employment Stimulus (ref. 2021.00391.CEECIND/CP1662/CT0003 DOI: https//doi.org/10.54499/2021.00391.CEECIND/CP1662/CT0003). This work received financial support from the PT national funds (FCT/MECI, Fundação para a Ciência e Tecnologia and Ministério da Educação, Ciência e Inovação) through the project UID/50006/2025 DOI 10.54499/UID/50006/2025 -Laboratório Associado para a Química Verde—Tecnologias e Processos Limpos.

REFERENCES

(1) Rettig, W. J.; Garin-Chesa, P.; Healey, J.; Su, S. L.; Ozer, H. L.; Schwab, M.; Albino, A. P.; Old, L. J. Regulation and Heteromeric Structure of the Fibroblast Activation Protein in Normal and Transformed Cells of Mesenchymal and Neuroectodermal Origin. *Cancer Res.* **1993**, *53* (14), 3327−3335.

(2) Jansen, K.; Heirbaut, L.; Verkerk, R.; Cheng, J. D.; Joossens, J.; Cos, P.; Maes, L.; Lambeir, A. M.; De Meester, I.; Augustyns, K.; Van Der Veken, P. Extended Structure-Activity Relationship and Pharmacokinetic Investigation of (4-Quinolinoyl)Glycyl-2-Cyanopyrrolidine Inhibitors of Fibroblast Activation Protein (FAP). *J. Med. Chem.* **2014**, *57* (7), 3053−3074.

(3) Loktev, A.; Lindner, T.; Burger, E. M.; Altmann, A.; Giesel, F.; Kratochwil, C.; Debus, J.; Marmé, F.; Jäger, D.; Mier, W.; Haberkorn, U. Development of Fibroblast Activation Protein−Targeted Radiotracers with Improved Tumor Retention. *J. Nucl. Med.* **2019**, *60* (10), 1421−1429.

(4) Hennrich, U.; Eder, M. [177Lu]Lu-PSMA-617 (PluvictoTM): The First FDA-Approved Radiotherapeutical for Treatment of Prostate Cancer. *Pharmaceuticals* **2022**, *15* (10), 1292.

(5) Brzeminski, P.; Verhulst, E.; Fabisiak, A.; Pacifico, R.; Willocx, D.; Peeters, S.; de Groot, A.; Corthaut, S.; Van Meel, K.; Stroobants, S.; Augustyns, K.; Berg, M.; Lambeir, A.-M.; Rösch, F.; De Meester, I.; Elvas, F.; Van der Veken, P. Structure−Property Investigation of New "KetoFAPI" Inhibitors of Fibroblast Activation Protein (FAP): Discovery of Highly Potent, Selective Compounds with Prolonged Residence Times and Promising Radiotheranostic Potential. *J. Med. Chem.* **2025**, *68* (20), 21739−21765.

(6) Verhulst, E.; Brzeminski, P.; de Groot, A.; Wals, J. W.; Michiels, R.; Fabisiak, A.; Thys, J.; Grintsevich, S.; Van Rymenant, Y.; Peeters, S.; Lambregts, S.; Sim, Y.; Verstraete, R.; Van Wielendaele, P.; Berg, M.; Elvas, F.; Van Ostade, X.; Rösch, F.; Lambeir, A.-M.; De Winter, H.; Van Der Veken, P.; De Meester, I. In Vitro Kinetic Profiling by Enzymatic Approaches to Select FAPIs with Long Residence Time. *Eur. J. Med. Chem.* **2026**, *304*, 118494.

(7) Warshel, A.; Karplus, M. Calculation of Ground and Excited State Potential Surfaces of Conjugated Molecules. I. Formulation and Parametrization. *J. Am. Chem. Soc.* **1972**, *94* (16), 5612−5625.

(8) Nobel Prize in Chemistry 2013; NobelPrize.org. Nobel Prize Outreach, 2025. https://www.nobelprize.org/prizes/chemistry/2013/summary/(accessed 10 31, 2025).

(9) Wang, Y. H.; Zhang, F.; Diao, H.; Wu, R. Covalent Inhibition Mechanism of Antidiabetic Drugs - Vildagliptin vs Saxagliptin. *ACS Catal.* **2019**, *9* (3), 2292−2302.

(10) Corredor, J. D.; Febres-Molina, C.; Jaña, G. A.; Jiménez, V. A. Insight into the Role of Active Site Protonation States and Water Molecules in the Catalytic Inhibition of DPP4 by Vildagliptin. *J. Chem. Inf. Model.* **2023**, *63* (4), 1338−1350.

(11) Nabeno, M.; Akahoshi, F.; Kishida, H.; Miyaguchi, I.; Tanaka, Y.; Ishii, S.; Kadowaki, T. A Comparative Study of the Binding Modes of Recently Launched Dipeptidyl Peptidase IV Inhibitors in the Active Site. *Biochem. Biophys. Res. Commun.* **2013**, *434* (2), 191−196.

(12) Park, J. E.; Lenter, M. C.; Zimmermann, R. N.; Garin-Chesa, P.; Old, L. J.; Rettig, W. J. Fibroblast Activation Protein, a Dual Specificity Serine Protease Expressed in Reactive Human Tumor Stromal Fibroblasts. *J. Biol. Chem.* **1999**, *274* (51), 36505−36512.

(13) Schnapp, G.; Hoevels, Y.; Bakker, R. A.; Schreiner, P.; Klein, T.; Nar, H. A Single Second Shell Amino Acid Determines Affinity and Kinetics of Linagliptin Binding to Type 4 Dipeptidyl Peptidase and Fibroblast Activation Protein. *ChemMedChem* **2021**, *16* (4), 630−639.

(14) Fiser, A.; Sali, A. ModLoop Automated Modeling of Loops in Protein Structures. *Bioinformatics* **2003**, *19* (18), 2500−2501.

(15) Williams, C. J.; Headd, J. J.; Moriarty, N. W.; Prisant, M. G.; Videau, L. L.; Deis, L. N.; Verma, V.; Keedy, D. A.; Hintze, B. J.; Chen, V. B.; Jain, S.; Lewis, S. M.; Arendall, W. B.; Snoeyink, J.; Adams, P. D.; Lovell, S. C.; Richardson, J. S.; Richardson, D. C. MolProbity: More and Better Reference Data for Improved All-Atom Structure Validation. *Protein Sci.* **2018**, *27* (1), 293−315.

(16) Anderson, M.; Moshnikova, A.; Engelman, D. M.; Reshetnyak, Y. K.; Andreev, O. A. Probe for the Measurement of Cell Surface PH in Vivo and Ex Vivo. *Proc. Natl. Acad. Sci. U.S.A.* **2016**, *113* (29), 8177−8181.

(17) Anandakrishnan, R.; Aguilar, B.; Onufriev, A. V. H++ 3.0: Automating PK Prediction and the Preparation of Biomolecular Structures for Atomistic Molecular Modeling and Simulations. *Nucleic Acids Res.* **2012**, *40* (W1), W537−W541.

(18) Søndergaard, C. R.; Olsson, M. H. M.; Rostkowski, M.; Jensen, J. H. Improved Treatment of Ligands and Coupling Effects in Empirical Calculation and Rationalization of PKa Values. *J. Chem. Theory Comput.* **2011**, *7* (7), 2284−2295.

(19) Olsson, M. H. M.; Søndergaard, C. R.; Rostkowski, M.; Jensen, J. H. PROPKA3: Consistent Treatment of Internal and Surface Residues in Empirical PKa Predictions. *J. Chem. Theory Comput.* **2011**, *7* (2), 525−537.

(20) *The PyMOL Molecular Graphics System*, Version 2.4.1. Schrödinger, LLC.

(21) Jorgensen, W. L.; Chandrasekhar, J.; Madura, J. D.; Impey, R. W.; Klein, M. L. Comparison of Simple Potential Functions for Simulating Liquid Water. *J. Chem. Phys.* **1983**, *79* (2), 926−935.

(22) Case, D. A.; et al. *Amber 2020*; University of California: San Francisco, 2020.

(23) Maier, J. A.; Martinez, C.; Kasavajhala, K.; Wickstrom, L.; Hauser, K. E.; Simmerling, C. Ff14SB: Improving the Accuracy of Protein Side Chain and Backbone Parameters from Ff99SB. *J. Chem. Theory Comput.* **2015**, *11* (8), 3696−3713.

(24) Wang, J.; Wolf, R. M.; Caldwell, J. W.; Kollman, P. A.; Case, D. A. Development and Testing of a General Amber Force Field. *J. Comput. Chem.* **2004**, *25* (9), 1157−1174.

(25) Fernandes, H. S.; Ramos, M. J.; Cerqueira, M. F. S. A. N. MolUP A VMD Plugin to Handle QM and ONIOM Calculations Using the Gaussian Software. *J. Comput. Chem.* **2018**, *39* (19), 1344−1353.

(26) Humphrey, W.; Dalke, A.; Schulten, K. VMD: Visual Molecular Dynamics. *J. Mol. Graphics* **1996**, *14* (1), 33−38.

(27) Frisch, M. J.; Trucks, G. W.; Schlegel, H. B.; Scuseria, G. E.; Robb, M. A.; Cheeseman, J. R.; Scalmani, G.; Barone, V.; Petersson, G. A.; Nakatsuji, H.; Li, X.; Caricato, M.; Marenich, A. V.; Bloino, J.; Janesko, B. G.; Gomperts, R.; Mennucci, B.; Hratchian, H. P.; Ortiz, J. V.; Izmaylov, A. F.; Sonnenberg, J. L.; Williams-Young, D.; Ding, F.; Lipparini, F.; Egidi, F.; Goings, J.; Peng, B.; Petrone, A.; Henderson, T.; Ranasinghe, D.; Zakrzewski, V. G.; Gao, J.; Rega, N.; Zheng, G.; Liang, W.; Hada, M.; Ehara, M.; Toyota, K.; Fukuda, R.; Hasegawa, J.; Ishida, M.; Nakajima, T.; Honda, Y.; Kitao, O.; Nakai, H.; Vreven, T.; Throssell, K.; Montgomery, J. A.; Peralta, J. E.; Ogliaro, F.; Bearpark, M. J.; Heyd, J. J.; Brothers, E. N.; Kudin, K. N.; Staroverov, V. N.; Keith, T. A.; Kobayashi, R.; Normand, J.; Raghavachari, K.; Rendell, A. P.; Burant, J. C.; Iyengar, S. S.; Tomasi, J.; Cossi, M.; Millam, J. M.; Klene, M.; Adamo, C.; Cammi, R.; Ochterski, J. W.; Martin, R. L.; Morokuma, K.; Farkas, O.; Foresman, J. B.; Fox, D. J. *Gaussian 16*, Revisions A.03 and C.01; Gaussian, Inc: Wallingford CT, 2016.

(28) Vreven, T.; Byun, K. S.; Komáromi, I.; Dapprich, S.; Montgomery, J. A.; Morokuma, K.; Frisch, M. J. Combining Quantum Mechanics Methods with Molecular Mechanics Methods in ONIOM. *J. Chem. Theory Comput.* **2006**, *2* (3), 815−826.

(29) Becke, A. D. Density-functional Thermochemistry. III. The Role of Exact Exchange. *J. Chem. Phys.* **1993**, *98* (7), 5648−5652.

(30) Stephens, P. J.; Devlin, F. J.; Chabalowski, C. F.; Frisch, M. J. Ab Initio Calculation of Vibrational Absorption and Circular Dichroism Spectra Using Density Functional Force Fields. *J. Phys. Chem.* **1994**, *98* (45), 11623−11627.

(31) Ditchfield, R.; Hehre, W. J.; Pople, J. A. Self-Consistent Molecular-Orbital Methods. IX. An Extended Gaussian-Type Basis for Molecular-Orbital Studies of Organic Molecules. *J. Chem. Phys.* **1971**, *54* (2), 724−728.

(32) Marenich, A. V.; Brothers, E. N.; Hratchian, H. P.; Frisch, M. J. Generalized Internal Coordinates for Creative Exploration of Interatomic Geometries. *J. Chem. Theory Comput.* **2025**, *21* (21), 10930−10944.

https://doi.org/10.1021/acs.jcim.6c00470
J. Chem. Inf. Model. 2026, 66, 7179−7189

(33) Hariharan, P. C.; Pople, J. A. The Influence of Polarization Functions on Molecular Orbital Hydrogenation Energies. *Theor. Chim. Acta* **1973**, *28*, 213−222.
(34) Grimme, S.; Antony, J.; Ehrlich, S.; Krieg, H. A Consistent and Accurate Ab Initio Parametrization of Density Functional Dispersion Correction (DFT-D) for the 94 Elements H-Pu. *J. Chem. Phys.* **2010**, *132* (15), 1−19.
(35) Aertgeerts, K.; Levin, I.; Shi, L.; Snell, G. P.; Jennings, A.; Prasad, G. S.; Zhang, Y.; Kraus, M. L.; Salakian, S.; Sridhar, V.; Wijnands, R.; Tennant, M. G. Structural and Kinetic Analysis of the Substrate Specificity of Human Fibroblast Activation Protein Alpha. *J. Biol. Chem.* **2005**, *280* (20), 19441−19444.
(36) Quesne, M. G.; Ward, R. A.; de Visser, S. P. Cysteine Protease Inhibition by Nitrile-Based Inhibitors: A Computational Study. *Front. Chem.* **2013**, *1* (39), 1−10.
(37) Dos Santos, A. M.; Cianni, L.; De Vita, D.; Rosini, F.; Leitão, A.; Laughton, C. A.; Lameira, J.; Montanari, C. A. Experimental Study and Computational Modelling of Cruzain Cysteine Protease Inhibition by Dipeptidyl Nitriles. *Phys. Chem. Chem. Phys.* **2018**, *20* (37), 24317−24328.
(38) Da Costa, C. H. S.; Bonatto, V.; Dos Santos, A. M.; Lameira, J.; Leitão, A.; Montanari, C. A. Evaluating QM/MM Free Energy Surfaces for Ranking Cysteine Protease Covalent Inhibitors. *J. Chem. Inf. Model.* **2020**, *60* (2), 880−889.
(39) Silva, J. R. A.; Cianni, L.; Araujo, D.; Batista, P. H. J.; De Vita, D.; Rosini, F.; Leitão, A.; Lameira, J.; Montanari, C. A. Assessment of the Cruzain Cysteine Protease Reversible and Irreversible Covalent Inhibition Mechanism. *J. Chem. Inf. Model.* **2020**, *60* (3), 1666−1677.
(40) Ramos-Guzmán, C. A.; Ruiz-Pernía, J. J.; Tuñón, I. Computational Simulations on the Binding and Reactivity of a Nitrile Inhibitor of the SARS-CoV-2 Main Protease. *Chem. Commun.* **2021**, *57* (72), 9096−9099.
(41) Aranda, J.; Wieczór, M.; Terrazas, M.; Brun-Heath, I.; Orozco, M. Mechanism of Reaction of RNA-Dependent RNA Polymerase from SARS-CoV-2. *Chem Catal.* **2022**, *2* (5), 1084−1099.
(42) Ngo, S. T.; Nguyen, T. H.; Tung, N. T.; Mai, B. K. Insights into the Binding and Covalent Inhibition Mechanism of PF-07321332 to SARS-CoV-2 M Pro. *RSC Adv.* **2022**, *12* (6), 3729−3737.
(43) Dos Santos, A. M.; Oliveira, A. R. S.; Da Costa, C. H. S.; Kenny, P. W.; Montanari, C. A.; Varela, J. D. J. G.; Lameira, J. Assessment of Reversibility for Covalent Cysteine Protease Inhibitors Using Quantum Mechanics/Molecular Mechanics Free Energy Surfaces. *J. Chem. Inf. Model.* **2022**, *62* (17), 4083−4094.
(44) Ramos-Guzmán, C. A.; Andjelkovic, M.; Zinovjev, K.; Ruiz-Pernía, J. J.; Tuñón, I. The Impact of SARS-CoV-2 3CL Protease Mutations on Nirmatrelvir Inhibitory Efficiency. Computational Insights into Potential Resistance Mechanisms. *Chem. Sci.* **2023**, *14* (10), 2686−2697.
(45) Grigorenko, B. L.; Polyakov, I. V.; Khrenova, M. G.; Giudetti, G.; Faraji, S.; Krylov, A. I.; Nemukhin, A. V. Multiscale Simulations of the Covalent Inhibition of the SARS-CoV-2 Main Protease: Four Compounds and Three Reaction Mechanisms. *J. Am. Chem. Soc.* **2023**, *145* (24), 13204−13214.
(46) Zaman, N.; Azam, S. S. Discrete Dynamics of Warhead Modulation on Covalent Inhibition of Oxyr: A QM/MM Study. *J. Phys. Chem. B* **2023**, *127* (27), 5993−6005.
(47) Oliva, A.; Henry, B.; Ruiz-López, M. F. Insights on Peptide Backbone N−H Acidity: Structure of Anions, Hydration Effects. *Chem. Phys. Lett.* **2013**, *561*−*562*, 153−158.
(48) Nsikabaka, S.; Harb, W.; Ruiz-López, M. F. The Role of Water on the Acid-Promoted E/Z Isomerization of Oximes in Aqueous Solution. *J. Mol. Struct.:THEOCHEM* **2006**, *764* (1−3), 161−166.
(49) Tolosa, S.; Mora-Diez, N.; Hidalgo, A.; Sansón, J. A. Amide-Imide Tautomerism of Acetohydroxamic Acid in Aqueous Solution: Quantum Calculation and SMD Simulations. *RSC Adv.* **2014**, *4* (84), 44757−44768.
(50) Grigorenko, B. L.; Khrenova, M. G.; Nemukhin, A. V. Amide−Imide Tautomerization in the Glutamine Side Chain in Enzymatic and Photochemical Reactions in Proteins. *Phys. Chem. Chem. Phys.* **2018**, *20* (37), 23827−23836.
(51) Jansen, K.; Heirbaut, L.; Cheng, J. D.; Joossens, J.; Ryabtsova, O.; Cos, P.; Maes, L.; Lambeir, A. M.; De Meester, I.; Augustyns, K.; Van Der Veken, P. Selective Inhibitors of Fibroblast Activation Protein (FAP) with a (4-Quinolinoyl)-Glycyl-2-Cyanopyrrolidine Scaffold. *ACS Med. Chem. Lett.* **2013**, *4* (5), 491−496.

https://doi.org/10.1021/acs.jcim.6c00470
J. Chem. Inf. Model. 2026, 66, 7179−7189